Elasticity of two-dimensional ferroelectrics across their paraelectric phase transformation

Joseph E. Roll [1], John M. Davis [1], John W. Villanova [1], and Salvador Barraza-Lopez [1,2,*]

[1]*Department of Physics, University of Arkansas, Fayetteville, Arkansas 72701, USA*

[2]*MonArk NSF Quantum Foundry, University of Arkansas, Fayetteville, Arkansas 72701, USA*

(Received 10 January 2022; revised 12 May 2022; accepted 2 June 2022; published 14 June 2022)

The mechanical behavior of two-dimensional (2D) materials across 2D phase changes is unknown, and the finite temperature (T) elasticity of paradigmatic SnSe monolayers—ferroelectric 2D materials turning paraelectric as their unit cell turns from a rectangle into a square—is described here in a progressive manner. To begin with, their zero-T total energy landscape gives way to (Boltzmann-like) averages from which the elastic behavior is determined. These estimates are complemented with results from the strain-fluctuation method, which employs the energy landscape or *ab initio* molecular dynamics data. All approaches capture the coalescence of elastic moduli $\langle C_{11}(T)\rangle = \langle C_{22}(T)\rangle$ due to the structural transformation. The broad evolution and sudden changes of elastic parameters $\langle C_{11}(T)\rangle$, $\langle C_{22}(T)\rangle$, and $\langle C_{12}(T)\rangle$ of these atomically thin phase-change membranes establishes a heretofore overlooked connection among 2D materials and soft matter.

DOI: 10.1103/PhysRevB.105.214105

I. INTRODUCTION

Two-dimensional (2D) materials have held promise as constituents in electronics, energy harvesting devices, spintronic applications, and optoelectronics [1–3]. Controlling their mechanical properties, one can tune their electronic and optical behavior [4]. Some 2D materials with rectangular unit cells –such as SnO or SnSe monolayers (MLs)—undergo structural transformations [5–8], and the same can be said of 2D metamaterials such as Ising-like puckered sheets [9]. The purpose of this paper is to predict sudden changes in elastic parameters on 2D materials undergoing phase transformations at finite temperature, whose magnitudes tend to be estimated only at zero temperature (zero T).

Understanding finite-T behavior is relevant, as zero-T estimates of elastic parameters (sometimes called elastic *constants*) lose meaning on materials undergoing phase transitions (transformations) at finite T, where elastic behavior is expected to change drastically. For example, zero-T elastic parameters $C_{11}^{(0)}$ and $C_{22}^{(0)}$ have different magnitudes on materials with a rectangular [or orthorhombic in three dimensions (3D)] unit cell, but these elastic moduli must turn identical at a critical T (T_c) in which the unit cell turns square (tetragonal, or cubic in 3D).

Noncentrosymmetric materials undergo nonaffine relaxations at finite temperature that result in softened elastic moduli [10,11]. Here, we present a study on the elastic behavior of SnSe MLs, noncentrosymmetric materials belonging to the group-IV monochalcogenide materials family. Group-IV monochalcogenide MLs are experimentally available [12–14] 2D ferroelectrics with a puckered rectangular unit cell and a $Pnm2_1$ group symmetry in their zero-T phase, whereby each atom is threefold coordinated [1,7,15–22]. They display metavalent bonding [23], characterized by large atomic effective charges, structural anharmonicity, and significant linear and nonlinear optical responses. Their low-T crystal structure also underpins anisotropic elasticity [24,25]. Nevertheless, these 2D materials undergo a firmly established structural change onto a fivefold coordinated square structure with $P4/nmm$ symmetry at a critical temperature T_c ranging between 200 and 300 K [7,12–14,20,21], at which their properties turn isotropic. Nothing has been said about the elastic behavior on their $P4/nmm$ phase yet, and approaches based on (i) an analytical form of the zero-T total energy landscape [26] and (ii) the strain-fluctuation method [27] are deployed to answer this open question here.

This paper is structured as follows: Computational methods are specified in Sec. II, and the results are provided in Sec. III. More specifically, the evolution of elasticity as obtained from second-order derivatives of the total energy landscape is reported in Sec. III A, while the results determined from the strain-fluctuation method are reported in Sec. III B. Conclusions are presented in Sec. IV.

II. METHODS

The total energy landscape and molecular dynamics (MD) data were calculated with the SIESTA density functional theory code [28,29] employing an exchange-correlation functional with self-consistent van der Waals corrections [30]. We employed the NPT ensemble here, as it permits lattice parameters a_1 and a_2 to vary. The experimentally observed phase transition on this material is triggered by a change in the rhombic angle $\Delta\alpha$ [12], which relates to a_1 and a_2 ($a_1 > a_2$) as $\frac{a_1}{a_2} - 1 = \Delta\alpha$ [20]. Other choices of ensemble that constrain the area of the material (e.g., the NVT ensemble) do not allow for lattice vectors (and hence ϵ_1 and ϵ_2) to change with temperature and thus are inconsistent with experimental observation (see Ref. [7] for an extended discussion). The *ab initio* MD

*sbarraza@uark.edu

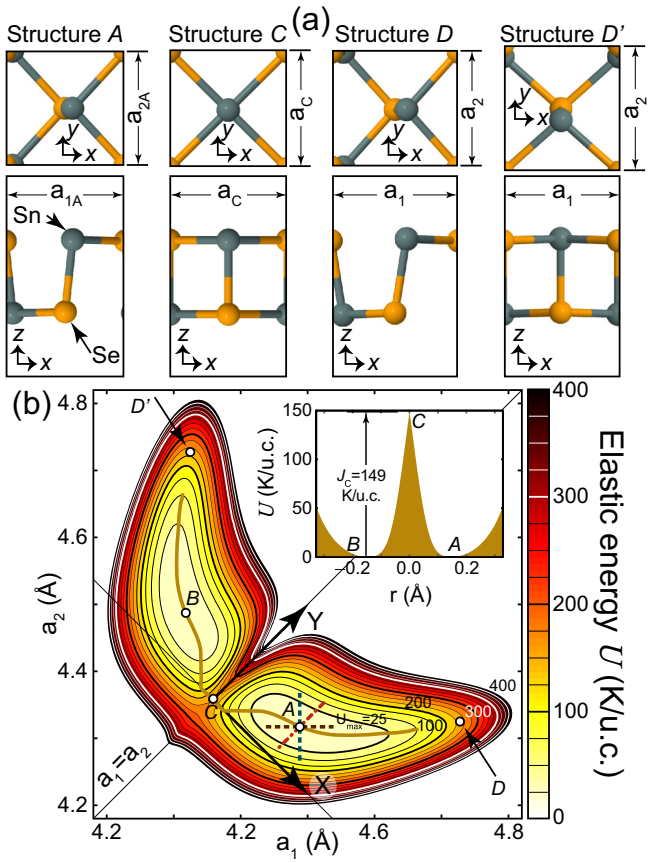

FIG. 1. (a) SnSe monolayer (ML) unit cell for points A, C, D, and D' on an analytical $U(a_1, a_2)$ [subplot (b)]. The solid curve connecting points A, C, and B on subplot (b) is the minimum-energy pathway among the two energy degenerate basins A and B, and the inset displays the energy barrier $J_C = U(a_C, a_C)$. Straight lines passing through point A were used to determine zero-T elastic moduli. Some isoenergy lines were drawn, too.

data was collected on samples containing 1024 atoms for at least 50 000 fs. Additional details can be found in Ref. [20].

III. RESULTS

A. Elasticity from the total energy landscape

As illustrated in Fig. 1(a), for a SnSe ML (a paradigmatic group-IV monochalcogenide ML), a crystal elongated or compressed along two orthogonal directions a_1 and a_2 with a subsequent structural optimization of atomic positions for given values of a_1 and a_2 leads to a zero-T total energy $E(a_1, a_2)$ per unit cell, which includes electronic, dipole, and elastic contributions. The change of energy $U(a_1, a_2) = E(a_1, a_2) - E(a_{1A}, a_{2A})$ with respect to a degenerate local minimum energy configuration—labeled A and having coordinates a_{1A} and a_{2A}—seen in Fig. 1(b) is a total energy landscape [31]. To simplify an eventual extraction of partial derivatives, the landscape $U(a_1, a_2)$ in Fig. 1(b) is an analytical fit to raw *ab initio* data [20]. The raw data sets an energy barrier separating the two degenerate minima equal to $J_{C,r} = 149.25$ K/u.c., lattice parameters $a_{1A,r} = 4.4873$ Å and $a_{2A,r} = 4.3264$ Å at the energy minima A, and $a_C = 4.3590$ Å for the square unit cell of lowest energy [20,32].

TABLE I. Fitting parameters for $U(X, Y)$. $J_C = 149$ K/u.c.

$\mathcal{U}_1$	−3660.5	±	12.3% K/Å^2
$\mathcal{U}_2$	24 849	±	4.3% K/Å^2
$\mathcal{U}_3$	−109 410	±	8.2% K/Å^3
$\mathcal{U}_4$	−42 945	±	21.2% K/Å^3
$\mathcal{U}_5$	188 100	±	9.2% K/Å^4
$\mathcal{U}_6$	114 840	±	43.4% K/Å^4
$\mathcal{U}_7$	−3568.5	±	13.4% K/Å
$\mathcal{U}_8$	−88 140	±	12.4% K/Å^2
g_1	0.0583	±	9.3% Å
g_2	0.0536	±	8.1% Å

Here, $U(a_1, a_2)$ is mirror symmetric with respect to the $a_1 = a_2$ line on Fig. 1(b), thus calling for new variables:

$$X = \frac{a_1 - a_2}{\sqrt{2}} \quad \text{and} \quad Y = \frac{a_1 + a_2 - 2a_C}{\sqrt{2}}, \tag{1}$$

where $X = 0$ and $Y = 0$ at point C (whose coordinates are $a_1 = a_2 = a_C$), which thus becomes the new origin of coordinates.

The mirror symmetry of the landscape about the $X = 0$ line makes $U(X, Y)$ even on X, and the following expression was used to fit numerical data [20]:

$$\begin{aligned} U(X, Y) = {} & J_C + \mathcal{U}_1 X^2 + \mathcal{U}_2 Y^2 + \mathcal{U}_3 Y X^2 + \mathcal{U}_4 Y^3 + \mathcal{U}_5 X^4 \\ & + \mathcal{U}_6 Y^4 + \left[\mathcal{U}_7 X \exp\left(-\frac{\sqrt{X^2}}{g_1}\right)\right. \\ & \left. + \mathcal{U}_8 Y X \exp\left(-\frac{\sqrt{X^2}}{g_2}\right)\right] \tanh(100X), \end{aligned} \tag{2}$$

with parameters and numerical uncertainties provided in Table I. With the exception of the terms on $\tanh(100X)$—whose sole purpose is to smooth the cusp observed at the barrier in the numerical data [20]; see inset of Fig. 1(b)—the total energy landscape is a polynomial of order four. The quality of the fitting can be ascertained by noticing that its minima A is located at $(a_{1A}, a_{2A}) = (4.4896$ Å, 4.3173 Å) [or $X_A = 0.1218$ Å, $Y_A = 0.0629$ Å], which is <0.25% different from the raw *ab initio* data. One also notices that the saddle point on $U(X, Y)$ (i.e., the minimum energy barrier separating the two ground states A and B) occurs exactly at point a_C as determined in the raw data and that $U(X_A, Y_A) = 0.0245$ K/u.c., leading to an energy barrier of 148.9755 K/u.c. which is only 0.2745 K/u.c. smaller than the one seen from the raw data.

Zero-T elastic moduli $C_{11}^{(0)}$, $C_{22}^{(0)}$, and $C_{12}^{(0)}$ are customarily obtained by fitting $U(a_1, a_2)$ to parabolas [24,25]:

$$U \simeq \mathfrak{U} = \frac{1}{2}\boldsymbol{\epsilon}^T C^{(0)} \boldsymbol{\epsilon} = \frac{C_{11}^{(0)}\epsilon_1^2}{2} + \frac{C_{22}^{(0)}\epsilon_2^2}{2} + C_{12}^{(0)}\epsilon_1\epsilon_2, \tag{3}$$

where strain coordinates $\boldsymbol{\epsilon} = (\epsilon_1, \epsilon_2)^T$, with

$$\epsilon_1 = \frac{a_1 - a_{1A}}{a_{1A}}, \qquad \epsilon_2 = \frac{a_2 - a_{2A}}{a_{2A}}, \tag{4}$$

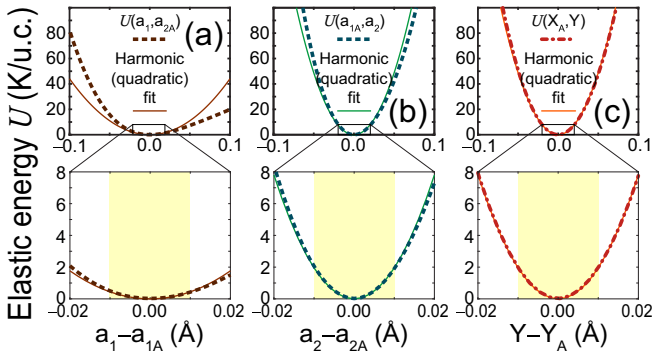

FIG. 2. Cuts of U along straight lines passing through point A on Fig. 1(b) and harmonic (i.e., quadratic) fits—thinner solid curves obtained within the shaded regions on the zoom-in plots—from which $C_{11}^{(0)}$, $C_{22}^{(0)}$, and $C_{12}^{(0)}$ were extracted.

were employed. We recall that a_{1A} and a_{2A} in Eq. (4) are zero-T equilibrium lattice parameters defining point A in the total energy landscape.

Here, $\mathcal{C}^{(0)}$ is the harmonic approximation to the elasticity tensor, and $\mathfrak{U}$ is the harmonic approximation to U. As acutely seen in Fig. 2(a), the prescription within Eq. (3) neglects the strong anharmonicity of group-IV monochalcogenide MLs by definition. Further, given that elastic moduli are thermodynamical averages after all, this approach misses a finite-T understanding of elasticity altogether.

Also, $U(X,Y)$ leads to zero-T elastic moduli consistent with prior work [24,25]: Eq. (2) is calculated along three straight lines [(a_1, a_{2A}), (a_{1A}, a_2), and (X_A, Y), corresponding to the brown (horizontal), green (vertical), and red (at 45°) straight lines passing through point A on Fig. 1(b), respectively], and Eq. (3) is fitted against the parabolas displayed on Fig. 2. Here, $C_{ij}^{(0)}$ are listed in Table II ($i, j = 1, 2$). Discrepancies with previous results (such as the smaller magnitude of $C_{11}^{(0)}$ and the slightly larger value of $C_{12}^{(0)}$ than $C_{11}^{(0)}$ here) are due to the use of different computational tools and exchange-correlation functionals in *ab initio* calculations. The softer $C_{11}^{(0)}$ here leads to a smaller T_c when contrasted to results using the numerical methods of Refs. [24,25]; see Refs. [7,21] for a discussion.

To go beyond the zero-T paradigm, we make use of $U(X,Y)$ to determine elastic behavior next. A function of X and Y has an expectation value within the total energy landscape $\langle f(U_{\max})\rangle$ as an average over classically accessible states [26]:

$$\langle f(U_{\max})\rangle = \frac{\oint \exp\left[-\frac{U(X,Y)}{U_{\max}}\right] f(X,Y)\,dX\,dY}{\oint \exp\left[-\frac{U(X,Y)}{U_{\max}}\right] dX\,dY}, \tag{5}$$

TABLE II. Zero-T in-plane elastic moduli (N/m).

Elastic modulus	Prior work	This paper
$C_{11}^{(0)}$	19.9 [24], 19.2 [25]	12.7
$C_{22}^{(0)}$	44.5 [24], 40.1 [25]	51.8
$C_{12}^{(0)}$	18.6 [24], 16.0 [25]	20.9

with $dX\,dY$ an area element within the confines of an isoenergy contour $U_{\max}$ around structure A, like those seen in Fig. 1(b).

Within this paradigm, $U(X,Y)$ is a classical potential energy profile, and a set of accessible crystalline configurations lies within isoenergy confines ($U_{\max}$ is the largest kinetic energy of a hypothetical particle in the landscape and is thus indirectly linked to T that way). For example, sampled unit cells will all have $a_1 > a_2$ when the $U_{\max}$ isoenergy curve is smaller than J_C. That is, the sampled structures will all be ferroelectric, having an in-plane polarization along the x direction [20]; see structure A in Fig. 1(a). When $U_{\max} \geqslant J_C$ nevertheless, the average structure encompasses minima A and B, yielding $a_1 = a_2$, and it thus is a square. The fact that $a_1 = a_2$ on average when $U_{\max} \geqslant J_C$ is illustrated by structures D and D' in Fig. 1(b), which have x and y coordinates swapped. In this sense, the averaging among crystalline configurations within the energy landscape up to an energy $U_{\max}$ achieves an effect like T: a transformation whereby the average unit cell turns from a rectangle into a square. A caveat to this model is that it is based on averaging over independent crystalline unit cells, while 2D structural transformations in 2D are driven by disorder [18,19].

Energy average values for C_{ij} are determined by [26]

$$\langle C_{ij}(U_{\max})\rangle = k_{\mathrm{B}}\left\{\left\langle \frac{\partial^2 u}{\partial\epsilon_i \partial\epsilon_j}\right\rangle - \frac{1}{U_{\max}}\left[\left\langle \mathcal{A}\frac{\partial u}{\partial\epsilon_i}\frac{\partial u}{\partial\epsilon_j}\right\rangle - \langle\mathcal{A}\rangle\left\langle\frac{\partial u}{\partial\epsilon_i}\right\rangle\left\langle\frac{\partial u}{\partial\epsilon_j}\right\rangle\right]\right\}, \tag{6}$$

with k_{B} Boltzmann's constant, $\mathcal{A} = a_1 a_2$, and $u = U/\mathcal{A}$.

Equation (6) was evaluated numerically for energy isovalues $U_{\max}$ starting at 1 K/u.c and up to 400 K/u.c. [Fig. 3(a)]. Near $U_{\max} = 0$, the averaging procedure yields elastic moduli smaller than those listed in Table II. Within this method, $\langle C_{12}\rangle$ quickly decays to a nearly zero value, and it becomes negative (for an auxetic behavior). On the other hand, $\langle C_{22}\rangle > \langle C_{11}\rangle$ by a factor in between 3 and 5 for energies up to $U_{\max} = J_C$, at which a sharp change occurs whereby $\langle C_{22}\rangle \approx \langle C_{11}\rangle$.

The fact that $\langle C_{22}\rangle \neq \langle C_{11}\rangle$ for isovalues $U_{\max} \geqslant J_C$, in which the average structure already turned isotropic [see Fig. 3(b)], represents an inaccuracy of the approach in Ref. [26]. It originates from the fact that strain was written out with respect to the zero-T ground state structure (a_{1A}, a_{2A}) in Eq. (4). Experimentally, strain at finite T is measured with respect to a structure in thermal equilibrium, calling for a calculation of elastic moduli in which average values of a_1 and a_2 are employed. Strain is then redefined as

$$\epsilon_1 = \frac{a_1 - \langle a_1\rangle}{\langle a_1\rangle} \quad \text{and} \quad \epsilon_2 = \frac{a_2 - \langle a_2\rangle}{\langle a_2\rangle}, \tag{7}$$

which is still valid at zero T in which $\langle a_i\rangle = a_{iA}$ ($i = 1, 2$). The resulting elastic parameters are shown in Fig. 3(c). Now $\langle C_{22}\rangle = \langle C_{11}\rangle$ for isovalues $U_{\max} \geqslant J_C$. The use of Eq. (7) instead of Eq. (4) is thus a correction to our previous method [26].

Here, $\langle C_{12}\rangle$ is the softest elastic modulus in this model. On the other hand, $\langle C_{11}\rangle$ hardens significantly at the transition ($U_{\max} = J_C$), while $\langle C_{22}\rangle$ suddenly softens at $U_{\max} = J_C$.

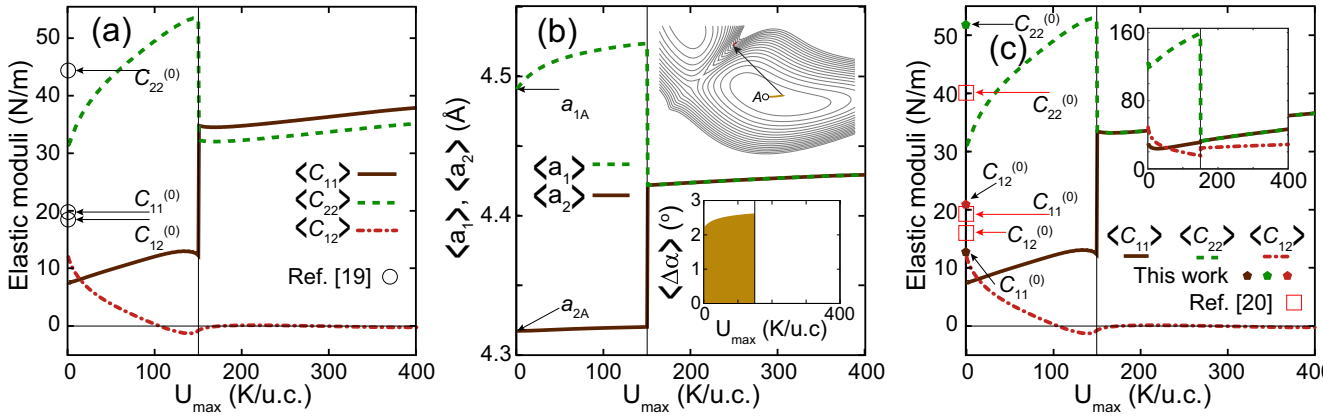

FIG. 3. (a) Elastic moduli as a function of $U_{\max}$ isovalue, setting the strain with respect to a_{1A} and a_{2A} at zero T. (b) Average lattice constants vs $U_{\max}$: the unit cell turns from a rectangle ($\langle a_1\rangle > \langle a_2\rangle$) into a square ($\langle a_1\rangle = \langle a_2\rangle$) when $U_{\max} \geqslant J_C$. Insets: Evolution of $\langle\Delta\alpha\rangle$ and of the point ($\langle a_1\rangle$, $\langle a_2\rangle$) vs $U_{\max}$. (c) Elastic moduli vs $U_{\max}$, setting the strain with respect to $\langle a_1\rangle$ and $\langle a_2\rangle$ as obtained at subplot (b): $\langle C_{11}\rangle = \langle C_{22}\rangle$ are now identical past J_C. Inset: Elastic moduli within the strain-fluctuation method. $C_{11}^{(0)}$, $C_{22}^{(0)}$, and $C_{12}^{(0)}$ as estimated by us and others are shown in subplots (a) and (c).

According to Fig. 3, a SnSe ML is much softer than graphene, for which $C_{11}^{(0)} = C_{22}^{(0)} = 336$ N/m and $C_{12}^{(0)} = 75$ N/m (see Ref. [33], and multiply by half of the unit cell thickness of Bernal graphite $\simeq 3.4$ Å).

We propose—by direct comparison of J_C and T_C from numerical calculations [21]—a linear correspondence between these two variables ($T \propto 1.42U_{\max}$) for this material, such that $T_C = 212$ K, and finite-T elastic behavior can be extracted from Fig. 3(c) at a low computational cost.

B. Elasticity from the strain-fluctuation method

We next employ the strain-fluctuation method to determine the elastic moduli. The expression to work with is [27]

$$\langle C^{-1}{}_{ij}\rangle = \frac{\langle\mathcal{A}\rangle}{k_B T}(\langle\epsilon_i\epsilon_j\rangle - \langle\epsilon_i\rangle\langle\epsilon_j\rangle), \tag{8}$$

which is less convoluted than Eq. (6) and also amenable for MD input.

Computed using $U(X,Y)$, $\langle\epsilon_i\rangle = \frac{\langle a_i\rangle - \langle a_i\rangle}{\langle a_i\rangle} = \frac{\langle a_i\rangle - \langle a_i\rangle}{\langle a_i\rangle} = 0$ ($i = 1, 2$) for additional simplification, and $\langle C_{ij}\rangle$ ($i, j = 1, 2$) are displayed as an inset on Fig. 3(c). One notes that $\langle C_{ij}\rangle > 0$ now, so that auxetic behavior cannot be confirmed within the strain-fluctuation method. A second point to notice is that $\langle C_{22}\rangle$ now becomes three times larger than its biggest magnitude obtained using Eq. (6). For $U_{\max} < J_C$, $\langle C_{11}\rangle$ is about twice as large as its magnitude from Eq. (6), too. Here, $\langle C_{11}\rangle = \langle C_{22}\rangle$ for $U_{\max} \geqslant J_C$, with a magnitude now comparable with that obtained from Eq. (6). The two takeaways from the strain-fluctuation approach [inset on Fig. 3(c)] are that $\langle C_{22}\rangle$ is much larger than its estimate using partial derivatives of $U(X,Y)$ and that $\langle C_{12}\rangle$ remains >0 .

The $Pnm2_1$-to-$P4/nmm$ structural transformation is signaled by a collapse of the rhombic distortion angle $\langle\Delta\alpha\rangle$ [related to a_1 and a_2 as $\langle\Delta\alpha\rangle = (\langle\frac{a_1}{a_2}\rangle - 1)\frac{180^\circ}{\pi}$] to a zero value [12,20]. As seen in the inset of Fig. 3(b), $U(X,Y)$ yields the required collapse of $\langle\Delta\alpha\rangle$, but it does not display a gradual decrease with a critical exponent of $\frac{1}{3}$ [12,20], as seen in the inset of Fig. 4(a)—obtained from MD. This is so because $U(X,Y)$ makes $\langle a_1\rangle$ plow to larger values, while $\langle a_2\rangle$ remains relatively unchanged up to $U_{\max} = J_C$, when both lattice parameters change discontinuously into an identical value [see Fig. 3(b) and its upper inset].

Thus, while an estimation of elastic properties based on $U(X,Y)$ [using either Eq. (6) or (8)] is relatively inexpensive, MD data were also utilized to estimate $\langle C_{11}\rangle$, $\langle C_{22}\rangle$, and $\langle C_{12}\rangle$ within the strain-fluctuation approach. Briefly, 16×16 supercells containing 1024 atoms were employed in NPT *ab initio* MD calculations for 16 different T between 100 and 400 K. Here, 20 000 individual time steps with a 1.5 fs resolution were obtained for each T. Thermal averages were obtained for times >5 ps to allow for proper thermalization. In this approach, $\epsilon_i = \frac{1}{2}[(\langle h\rangle^{-1T} h^T h \langle h\rangle^{-1})_{ii} - 1]$ ($i = 1, 2$) [27]. Here, $h = (\mathbf{a}_1, \mathbf{a}_2)$ and $\langle h\rangle = (\langle\mathbf{a}_1\rangle, \langle\mathbf{a}_2\rangle)$ are 2×2 matrices containing the in-plane magnitudes of supercell lattice vectors $\mathbf{a}_1$ and $\mathbf{a}_2$, which are written in column form. The matrix h contains the in-plane superlattice constants for one MD step, and $\langle h\rangle$ is its average over the available MD steps past thermalization. Here, $\langle\mathcal{A}\rangle$ is replaced by the area thermal average of the supercell.

The results, shown in Figs. 4(b) and 4(c), indicate a magnitude of $\langle C_{22}\rangle$ comparable with that of graphene at 100 K [33] but a softer magnitude of $\langle C_{11}\rangle$ that is four times smaller, as expected due to the anisotropy of the SnSe ML. All elastic constants then decrease, in a manner like that seen in the inset of Fig. 3(c). Here, $\langle C_{ii}\rangle$ ($i = 1, 2$) turn similar despite the method employed at energies/temperatures above the transition.

IV. CONCLUSIONS

The finite-T elastic behavior of a paradigmatic 2D ferroelectric was estimated from second-order partial derivatives of the energy on their zero-T total energy landscape and following the prescriptions of the strain-fluctuation method as well. Within the latter method, average strain was introduced utilizing either the total energy landscape or dedicated

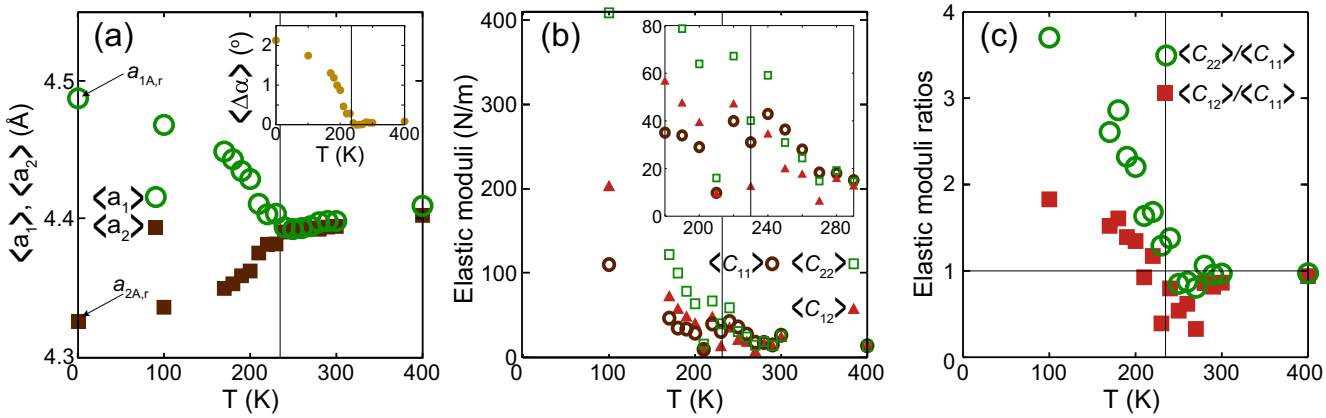

FIG. 4. (a) $\langle a_1 \rangle$ and $\langle a_2 \rangle$ vs T in molecular dynamics (MD) calculations. Inset: $\langle \Delta\alpha \rangle$. (b) Elastic moduli from the strain-fluctuation method and $\langle \epsilon_i \epsilon_j \rangle$, $\langle \epsilon_i \rangle$ $(i = 1, 2)$ determined from MD: see the coalescence of $\langle C_{11} \rangle$ and $\langle C_{22} \rangle$ past T_C, and the similar magnitudes of $\langle C_{ij} \rangle$ to those seen in the inset of Fig. 3(c). (c) Ratio among the elastic moduli displayed in subplot (b).

ab initio MD data. Regardless of method, $\langle C_{11} \rangle$ are shown to coalesce past the transition energy J_C or temperature T_C, and the elastic moduli turn much softer than that determined on graphene. The results contained here thus show how to understand the finite-T elastic behavior of 2D materials undergoing 2D transformations.

ACKNOWLEDGMENTS

The authors acknowledge Dr. P. Kumar for insightful conversations, as well as support from the U.S. Department of Energy (J.W.V. was funded by Award No. DE-SC0016139 and S.B.L. by Award No. DE-SC0022120).

[1] C. Cui, F. Xue, W.-J. Hu, and L.-J. Li, npj 2D Mater. Appl. **2**, 18 (2018).
[2] H. Zeng, J. Dai, W. Yao, D. Xiao, and X. Cui, Nat. Nanotechnol. **7**, 490 (2012).
[3] A. K. Geim and I. V. Grigorieva, Nature (London) **499**, 419 (2013).
[4] P. Z. Hanakata, A. Carvalho, D. K. Campbell, and H. S. Park, Phys. Rev. B **94**, 035304 (2016).
[5] L. Seixas, A. S. Rodin, A. Carvalho, and A. H. Castro Neto, Phys. Rev. Lett. **116**, 206803 (2016).
[6] T. B. Bishop, E. E. Farmer, A. Sharmin, A. Pacheco-Sanjuan, P. Darancet, and S. Barraza-Lopez, Phys. Rev. Lett. **122**, 015703 (2019).
[7] S. Barraza-Lopez, B. M. Fregoso, J. W. Villanova, S. S. P. Parkin, and K. Chang, Rev. Mod. Phys. **93**, 011001 (2021).
[8] W. Li, X. Qian, and J. Li, Nat. Rev. Mater. **6**, 829 (2021).
[9] P. Z. Hanakata, A. Plummer, and D. R. Nelson, Phys. Rev. Lett. **128**, 075902 (2022).
[10] B. Cui, A. Zaccone, and D. Rodney, J. Chem. Phys. **151**, 224509 (2019).
[11] A. Zaccone and E. M. Terentjev, Phys. Rev. Lett. **110**, 178002 (2013).
[12] K. Chang, J. Liu, H. Lin, N. Wang, K. Zhao, A. Zhang, F. Jin, Y. Zhong, X. Hu, W. Duan *et al.*, Science **353**, 274 (2016).
[13] K. Chang, F. Küster, B. J. Miller, J.-R. Ji, J.-L. Zhang, P. Sessi, S. Barraza-Lopez, and S. S. P. Parkin, Nano Lett. **20**, 6590 (2020).
[14] N. Higashitarumizu, H. Kawamoto, C.-J. Lee, B.-H. Lin, F.-H. Chu, I. Yonemori, T. Nishimura, K. Wakabayashi, W.-H. Chang, and K. Nagashio, Nat. Commun. **11**, 2428 (2020).
[15] Y. Ye, Q. Guo, X. Liu, C. Liu, J. Wang, Y. Liu, and J. Qiu, Chem. Mater. **29**, 8361 (2017).
[16] M. Wu and P. Jena, WIREs Comput. Mol. Sci. **8**, e1365 (2018).
[17] Z. Guan, H. Hu, X. Shen, P. Xiang, N. Zhong, J. Chu, and C. Duan, Adv. Electron. Mater. **6**, 1900818 (2020).
[18] M. Mehboudi, A. M. Dorio, W. Zhu, A. van der Zande, H. O. H. Churchill, A. A. Pacheco-Sanjuan, E. O. Harriss, P. Kumar, and S. Barraza-Lopez, Nano Lett. **16**, 1704 (2016).
[19] M. Mehboudi, B. M. Fregoso, Y. Yang, W. Zhu, A. van der Zande, J. Ferrer, L. Bellaiche, P. Kumar, and S. Barraza-Lopez, Phys. Rev. Lett. **117**, 246802 (2016).
[20] S. Barraza-Lopez, T. P. Kaloni, S. P. Poudel, and P. Kumar, Phys. Rev. B **97**, 024110 (2018).
[21] J. W. Villanova, P. Kumar, and S. Barraza-Lopez, Phys. Rev. B **101**, 184101 (2020).
[22] J. W. Villanova and S. Barraza-Lopez, Phys. Rev. B **103**, 035421 (2021).
[23] I. Ronneberger, Z. Zanolli, M. Wuttig, and R. Mazzarello, Adv. Mater. **32**, 2001033 (2020).
[24] R. Fei, W. Li, J. Li, and L. Yang, Appl. Phys. Lett. **107**, 173104 (2015).
[25] L. C. Gomes, A. Carvalho, and A. H. Castro Neto, Phys. Rev. B **92**, 214103 (2015).
[26] A. Pacheco-Sanjuan, T. B. Bishop, E. E. Farmer, P. Kumar, and S. Barraza-Lopez, Phys. Rev. B **99**, 104108 (2019).
[27] J. R. Ray, Comput. Phys. Rep. **8**, 109 (1988).
[28] R. M. Martin, *Electronic Structure: Basic Theory and Practical Methods* (Cambridge University Press, Cambridge, 2004).
[29] J. M. Soler, E. Artacho, J. D. Gale, A. García, J. Junquera, P. Ordejón, and D. Sánchez-Portal, J. Phys.: Condens. Matter **14**, 2745 (2002).

[30] G. Román-Pérez and J. M. Soler, Phys. Rev. Lett. **103**, 096102 (2009).

[31] D. J. Wales, *Energy Landscapes: Applications to Clusters, Biomolecules and Glasses* (Cambridge University Press, Cambridge, 2003).

[32] S. P. Poudel, J. W. Villanova, and S. Barraza-Lopez, Phys. Rev. Materials **3**, 124004 (2019).

[33] S. Thomas, K. Ajith, S. U. Lee, and M. C. Valsakumar, RSC Adv. **8**, 27283 (2018).